Sliding Mode Current Control of Mutually Coupled Switched Reluctance Machines using a Three-phase Voltage Source Converter

Kun Hu, Jin Ye, and Javad Mohammadpour Velni
School of Electrical and Computer Engineering
University of Georgia, Athens, Georgia 30602
Email: kun.hu@uga.edu, jin.ye@uga.edu, javadm@uga.edu

***Abstract*—In this paper, a sliding mode current controller (SMC) is proposed for mutually coupled switched reluctance machines (MCSRMs) using a three-phase voltage source converter (VSC). A generalized state-space model of MCSRMs is first presented using a three-phase voltage source converter. Asymmetric bridge converters and three-phase voltage source converter are compared in terms of switching frequency. A sliding mode current controller is then designed to achieve constant switching frequency and lower sampling rate using a three-phase VSC. The stability analysis of the sliding controller is given to ensure the stability of the controller. Finally, the effectiveness of SMC is verified through simulation studies with a three-phase, sinusoidal excitation 12/8 MCSRM over a wide speed range. Compared to the hysteresis current control, SMC demonstrates a comparable performance in terms of torque ripples, torque root-mean-square tracking errors (RMSE) and current RMSE while achieving a constant switching frequency and much lower sampling rate.**

***Index Terms*—mutually coupled switched reluctance motors, sliding mode current control, three-phase voltage source converter, asymmetric bridge converter**

I. Introduction

Switched reluctance motors (SRMs) (Fig. 1) are currently emerging as a promising alternative to permanent magnet (PM) machines in electrified transportation, industrial applications, and home appliances, primarily due to their rigidity, non-reliance on rare-earth permanent magnet materials, and extended-speed constant-power range [1]–[4]. Retaining the above important benefits of conventional switched reluctance machines (CSRMs), mutually coupled switched reluctance motors (MCSRMs) offer further distinctive advantages, for instance, lower copper and iron losses, higher fault tolerance and less sensitivity to magnetic saturation [5]–[8].

Unlike CSRMs, MCSRMs utilize both self inductance and mutual inductance between phases to generate electromagnetic torque, and thus two or three phases should be energized simultaneously. Therefore, with a flexible excitation scheme, MCSRMs can be driven by a three-phase voltage source converter (VSC) with either bipolar square-waveform or sinusoidal-waveform current excitation [9]. Previous related work [10], [11] only focused on the acoustic noise and mechanical vibration reduction for CSRMs. Authors in [12] first numerically demonstrated that sinusoidal current excitation shows promise in acoustic noise reduction for MCSRMs.

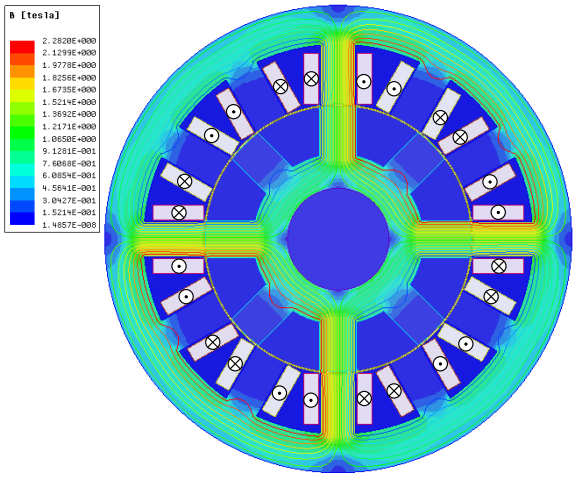

Fig. 1 Conventional SRM.

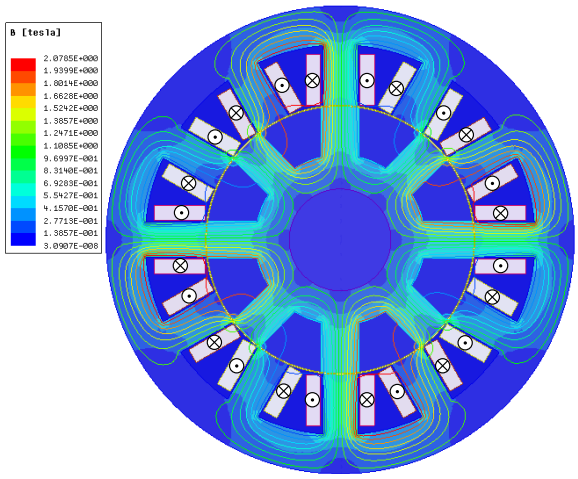

Fig. 2 Short-pitched MCSRM.

Current hysteresis control is widely used in SRM drives due to its simplicity, fast dynamic response and independence of machine models. However, this method suffers from variable switching frequency and much higher sampling rate in the digital implementation. To overcome these deficiencies, constant-switching-frequency current controllers were developed in [3]

for CSRMs; however, constant switching frequency current control for MCSRMs has yet to be explored because of the extreme nonlinearity and mutual coupling. The more relevant work is on the sliding mode current control for CSRMs [13]–[15], in which the relatively weak mutual coupling impact is not considered. Therefore, previous works cannot be directly applied to MCSRMs because of significant mutual coupling. Generally speaking, MCSRMs can be categorized as short-pitched (Fig. 2), full-pitched and fractionally-pitched MCSRMs, and each has unique flux and torque characteristics due to different winding distributions. In this paper, through the design and tuning of the sliding mode controller, a constant switching frequency current controller is developed for a short-pitched MCSRM to address the above issues.

The paper is organized as follows. In section II, mathematical modeling of a three-phase 12/8 MCSRM driven by a VSC is first presented. Then, the advantage of employing a three-phase VSC for reducing switching frequency is studied. Section III presents the problem formulation of the sliding mode control, wherein the variable switching frequency issue caused by traditional hysteresis current controllers is addressed. Moreover, to demonstrate the robustness of sliding mode controller, stability analysis of the closed-loop system is presented. Then, comparison results are shown in section IV to validate the effectiveness of the proposed sliding mode current controller, and conclusions are given in Section V.

II. Modeling Of MCSRMs

The terminal voltage equations (see [3]) for a three-phase MCSRM driven by a standard VSC shown in Fig. 3 are given by

$$\begin{bmatrix} v_{k-1} \\ v_k \\ v_{k+1} \end{bmatrix} = H \begin{bmatrix} i_{k-1} \\ i_k \\ i_{k+1} \end{bmatrix} + \Lambda \begin{bmatrix} \frac{d}{dt} i_{k-1} \\ \frac{d}{dt} i_k \\ \frac{d}{dt} i_{k+1} \end{bmatrix} \tag{1}$$

wherein the mutual inductances at non-primary diagonal positions in the coefficient matrices H and Λ reflect the mutual coupling between phases. The matrices H and Λ are defined as

$$H = \begin{bmatrix} R + \frac{\partial L_{k-1}}{\partial \theta}\omega_m & \frac{\partial M_{k(k-1)}}{\partial \theta}\omega_m & \frac{\partial M_{(k-1)(k+1)}}{\partial \theta}\omega_m \\ \frac{\partial M_{k(k-1)}}{\partial \theta}\omega_m & R + \frac{\partial L_k}{\partial \theta}\omega_m & \frac{\partial M_{k(k+1)}}{\partial \theta}\omega_m \\ \frac{\partial M_{(k-1)(k+1)}}{\partial \theta}\omega_m & \frac{\partial M_{k(k+1)}}{\partial \theta}\omega_m & R + \frac{\partial L_{k+1}}{\partial \theta}\omega_m \end{bmatrix},$$

$$\Lambda = \begin{bmatrix} L_{k-1} & M_{k(k-1)} & M_{(k-1)(k+1)} \\ M_{k(k-1)} & L_k & M_{k(k+1)} \\ M_{(k-1)(k+1)} & M_{k(k+1)} & L_{k+1} \end{bmatrix},$$

where v_{k-1}, v_k, v_{k+1} are terminal voltages and equivalent to the phase-to-neutral voltages v_{AO}, v_{BO}, v_{CO} defined in Fig. 3, respectively; R is ohmic resistance; i_j, L_j are phase current, and self inductance of jth phase $(j = k-1, k, k+1)$, respectively; θ is rotor angle; and ω_m is angular speed. Since the mutual inductances between two conducting phases are the same, e.g., $M_{(k-1)(k+1)} = M_{(k+1)(k-1)}$, we use

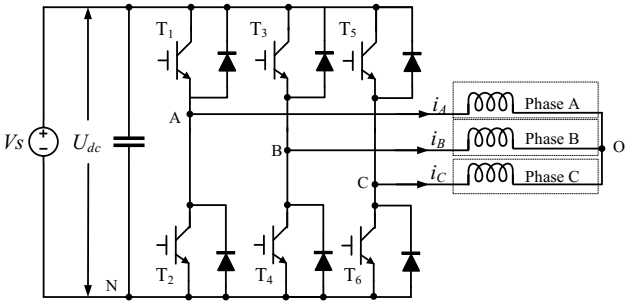

Fig. 3 Three-phase standard VSC.

$M_{(k-1)k}, M_{(k-1)(k+1)}$ and $M_{k(k+1)}$ to denote the mutual inductances among the adjacent conducting phases.

The electromagnetic torque of the MCSRM is produced from the variation of mutual inductance and self inductance. The studied MCSRM is designed to be less sensitive to magnetic saturation, which is demonstrated by the inductance profiles from ANSYS in Fig. 4. Therefore, the total electromagnetic torque of the n-phase MCSRM working in the linear magnetic region is given by

$$\begin{aligned} T = & \frac{1}{2}\frac{\partial L_{k-1}}{\partial \theta} i_{k-1}^2 + \frac{1}{2}\frac{\partial L_k}{\partial \theta} i_k^2 \\ & + \frac{1}{2}\frac{\partial L_{k+1}}{\partial \theta} i_{k+1}^2 + \frac{\partial M_{k(k-1)}}{\partial \theta} i_{k-1} i_k \\ & + \frac{\partial M_{k(k+1)}}{\partial \theta} i_k i_{k+1} + \frac{\partial M_{(k-1)(k+1)}}{\partial \theta} i_{k-1} i_{k+1}. \end{aligned} \tag{2}$$

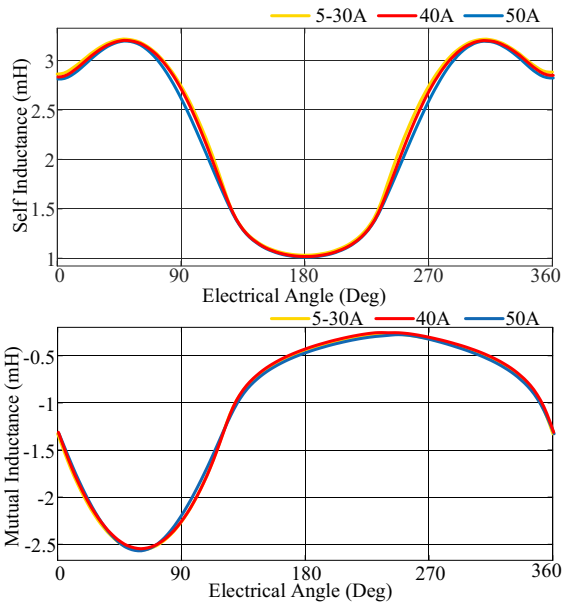

Fig. 4 Inductance profiles of the studied MCSRM.

The relation between phase voltages v_{AO}, v_{BO}, v_{CO} and inverter leg voltages v_{AN}, v_{BN}, v_{CN} in a balanced system is

as follows

$$\begin{bmatrix} v_{AO} \\ v_{BO} \\ v_{CO} \end{bmatrix} = \begin{bmatrix} \frac{2}{3} & -\frac{1}{3} & -\frac{1}{3} \\ -\frac{1}{3} & \frac{2}{3} & -\frac{1}{3} \\ -\frac{1}{3} & -\frac{1}{3} & \frac{2}{3} \end{bmatrix} \begin{bmatrix} v_{AN} \\ v_{BN} \\ v_{CN} \end{bmatrix}. \quad (3)$$

After we obtain the control signal (terminal voltage) from the controller, we then determine the inverter leg voltage to generate PWM signals. As switching frequency is an important factor in evaluating the performance of the converter, in this section, we compare the switching frequency of the VSC and the asymmetric bridge converter for the same MCSRM.

The switching frequency reaches its maximum when the back electromotive force (EMF) is neglected, and hence kth phase voltage is derived by

$$v_k \approx L_k \frac{di_k}{dt} + M_{k(k-1)} \frac{di_{k-1}}{dt} + M_{k(k+1)} \frac{di_{k+1}}{dt}, \quad (4)$$

wherein the three-phase currents are confined by Y connection as:

$$i_k + i_{k-1} + i_{k+1} = 0. \quad (5)$$

Assuming that the switching frequencies for the three phases are the same and that the absolute value of the current ripple for the three phases are the same, the highest switching frequency f_k is obtained when the denominator reaches the lowest value in (6).

$$f_k \approx \frac{v_k}{2\Big((-1)^l L_k + (-1)^m M_{k(k+1)} + (-1)^n M_{k(k-1)}\Big)\Delta i_k}, \quad (6)$$

where l, m and n are not all even or all odd integers.

Referring to the finite element analysis (FEA) result of the studied MCSRM, $((-1)^l L_k + (-1)^m M_{k(k+1)} + (-1)^n M_{k(k-1)})$ at every time instant varies between 0.67mH and 6.3mH, which leads to a maximum 53 kHz switching frequency and minimum 5.7 kHz switching frequency when the current band is 1 A and DC voltage is 72 V. The switching frequency would be much higher if the machine is driven by an asymmetric bridge converter [16]. In this case, the current derivatives for three phases can have the same sign (either positive or negative). Then $(L_k + M_{k(k+1)} + M_{k(k-1)})$, i.e., the denominator in (6), is lower, hence generating much higher switching frequency. As pointed out in [16], the sum of $L_k, M_{k(k+1)}$ and $M_{k(k-1)}$ at every time instant varies from 190μH to 720μH, which leads to a minimum 50 kHz switching frequency under the same condition. Therefore, employing the VSC significantly reduces the switching frequency compared to the conventional asymmetric bridge converter.

III. Sliding Mode Current Controller

In this section, we describe the design process of the proposed SMC-based controller and then provide stability analysis for the closed-loop system. The current control diagram is shown in Fig. 5.

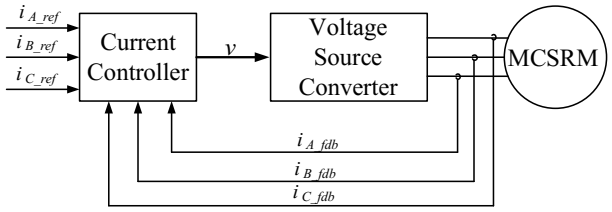

Fig. 5 Current control diagram.

A. Design of sliding mode controller

To address the variable switching frequency issue for MCSRMs, sliding mode current controller is proposed in this work. Based on the terminal voltage equation (1), the state-space dynamics of the current control system can be derived as

$$\dot{e} = -Ae + Ai_{ref} - Bv, \quad (7)$$

where the current errors associated with the three phases form the state vector e, the voltages associated with the three phases form the control input vector v, and A, B and e are defined as

$$A = BH,\ B = \Lambda^{-1}, v = \begin{bmatrix} v_{k-1} & v_k & v_{k+1} \end{bmatrix}^T,$$
$$e = \begin{bmatrix} e_{k-1} \\ e_k \\ e_{k+1} \end{bmatrix} = \begin{bmatrix} i_{ref_{k-1}} - i_{k-1} \\ i_{ref_k} - i_k \\ i_{ref_{k+1}} - i_{k+1} \end{bmatrix}.$$

An integral switching surface for the conducting phases is chosen as

$$\sigma(t) = e(t) + \alpha \int e(t)dt. \quad (8)$$

To force σ to slide along the restricted sliding surface σ = 0, the dynamics of the sliding mode σ are designed as follows:

$$\dot{\sigma} = -q\sigma + \varepsilon \text{sgn}(\sigma) \quad (9)$$

with

$$\varepsilon = \begin{bmatrix} \varepsilon_{k-1} & 0 & 0 \\ 0 & \varepsilon_k & 0 \\ 0 & 0 & \varepsilon_{k+1} \end{bmatrix},\ \sigma = \begin{bmatrix} \sigma_{k-1} & \sigma_k & \sigma_{k+1} \end{bmatrix}^T,$$
$$\alpha = \begin{bmatrix} \alpha_{k-1} & 0 & 0 \\ 0 & \alpha_k & 0 \\ 0 & 0 & \alpha_{k+1} \end{bmatrix},\ q = \begin{bmatrix} q_{k-1} & 0 & 0 \\ 0 & q_k & 0 \\ 0 & 0 & q_{k+1} \end{bmatrix},$$
$$\text{sgn}(\sigma) = \begin{bmatrix} \text{sgn}(\sigma_{k-1}) & \text{sgn}(\sigma_k) & \text{sgn}(\sigma_{k+1}) \end{bmatrix}^T,$$

in which the gains a, q, ε for each phase are positive to ensure the convergence of sliding mode and current error. Then, by combing (7)-(9), the control input v can be derived as

$$v = B^{-1}(q\sigma + \varepsilon \text{sgn}(\sigma) + \alpha e - Ae + Ai_{ref}). \quad (10)$$

To obtain the duty cycle d of the PWM control for each phase, the pseudoinverse of the coefficient matrix in (3) is applied

to construct the solution of a minimum Euclidean norm for $\begin{bmatrix} v_{AN} & v_{BN} & v_{CN} \end{bmatrix}^T$ as

$$\begin{bmatrix} d_{k-1} \\ d_k \\ d_{k+1} \end{bmatrix} = \frac{1}{v_{dc}} \begin{bmatrix} v_{AN} \\ v_{BN} \\ v_{CN} \end{bmatrix} = \begin{bmatrix} \frac{2}{3} & -\frac{1}{3} & -\frac{1}{3} \\ -\frac{1}{3} & \frac{2}{3} & -\frac{1}{3} \\ -\frac{1}{3} & -\frac{1}{3} & \frac{2}{3} \end{bmatrix}^{-1} \frac{v}{v_{dc}}, \tag{11}$$

where v_{dc} denotes the DC link voltage.

B. Stability analysis of the closed-loop system

When the motor parameter uncertainties are neglected, the closed-loop system dynamics can be derived by combining the current error dynamics and sliding mode control dynamics as

$$\dot{X} = A_1 X + B_1 U, \tag{12}$$

where B_1 is the identity matrix, and X, U and A_1 are defined as

$$X = \begin{bmatrix} s_{k-1} \\ s_k \\ s_{k+1} \\ e_{k-1} \\ e_k \\ e_{k+1} \end{bmatrix}, \quad U = \begin{bmatrix} -\varepsilon_{k-1}\mathrm{sgn}(s_{k-1}) \\ -\varepsilon_k \mathrm{sgn}(s_k) \\ -\varepsilon_{k+1}\mathrm{sgn}(s_{k+1}) \\ e_{k-1} \\ e_k \\ e_{k+1} \end{bmatrix},$$

$$A_1 = \begin{bmatrix} -q_{k-1} & 0 & 0 & 0 & 0 & 0 \\ 0 & -q_k & 0 & 0 & 0 & 0 \\ 0 & 0 & -q_{k+1} & 0 & 0 & 0 \\ -q_{k-1} & 0 & 0 & -\alpha_{k-1} & 0 & 0 \\ 0 & -q_k & 0 & 0 & -\alpha_k & 0 \\ 0 & 0 & -q_{k+1} & 0 & 0 & -\alpha_{k+1} \end{bmatrix}.$$

Then, the stability of the system in (12) can be proved using Lyapunov stability theory as follows. The Lyapunov function is chosen as

$$V(X) = X^T P X, \tag{13}$$

where P is a positive definite matrix and satisfies

$$A_1^T P + P A_1 = -I. \tag{14}$$

Then, the first-order derivative of $V(X)$ is

$$\begin{aligned} \dot{V}(X) &= \dot{X}^T P X + X^T P \dot{X} \\ &= \dot{X}(A_1^T P + P A_1) X + 2U^T B_1^T P X \\ &= -||X||^2 + 2U^T B_1^T P X. \end{aligned} \tag{15}$$

If U in the above equations is bounded and X is large enough, $\dot{V}(X)$ is then negative. In other words, bounded X can make the system bounded-input and bounded-output (BIBO) stable. Therefore, to ensure the BIBO stability, a positive definite P should be obtained by solving (14), which gives

$$P = \begin{bmatrix} p_{11} & 0 & 0 & p_{14} & 0 & 0 \\ 0 & p_{22} & 0 & 0 & p_{25} & 0 \\ 0 & 0 & p_{33} & 0 & 0 & p_{36} \\ p_{41} & 0 & 0 & p_{44} & 0 & 0 \\ 0 & p_{52} & 0 & 0 & p_{55} & 0 \\ 0 & 0 & p_{63} & 0 & 0 & p_{66} \end{bmatrix} \tag{16}$$

where

$$\begin{aligned} p_{11} &= \frac{(\alpha_{k-1}+q_{k-1})\alpha_{k-1}+q_{k-1}^2}{2(\alpha_{k-1}+q_{k-1})\alpha_{k-1}q_{k-1}}, p_{44} = \frac{1}{2\alpha_{k-1}}, \\ p_{22} &= \frac{(\alpha_k+q_k)\alpha_k+q_k^2}{2(\alpha_k+q_k)\alpha_k q_k}, p_{55} = \frac{1}{2\alpha_k}, \\ p_{33} &= \frac{(\alpha_{k+1}+q_{k+1})\alpha_{k+1}+q_{k+1}^2}{2(\alpha_{k+1}+q_{k+1})\alpha_{k+1}q_{k+1}}, p_{66} = \frac{1}{2\alpha_{k+1}}, \\ p_{14} &= p_{41} = \frac{-q_{k-1}}{2(\alpha_{k-1}+q_{k-1})\alpha_{k-1}q_{k-1}}, \\ p_{25} &= p_{52} = \frac{-q_k}{2(\alpha_k+q_k)\alpha_k q_k}, \\ p_{36} &= p_{63} = \frac{-q_{k+1}}{2(\alpha_{k+1}+q_{k+1})\alpha_{k+1}q_{k+1}}. \end{aligned}$$

To ensure that P is positive definite, selection of the parameters α and q for the sliding mode controller is guided with the following conditions:

$$\begin{aligned} &\frac{(\alpha_{k-1}+q_{k-1})\alpha_{k-1}+q_{k-1}^2}{2(\alpha_{k-1}+q_{k-1})\alpha_{k-1}q_{k-1}} > 0, \ \frac{(\alpha_k+q_k)\alpha_k+q_k^2}{2(\alpha_k+q_k)\alpha_k q_k} > 0, \\ &\frac{(\alpha_{k+1}+q_{k+1})\alpha_{k+1}+q_{k+1}^2}{2(\alpha_{k+1}+q_{k+1})\alpha_{k-1}q_{k-1}} > 0, \\ &\frac{(\alpha_{k-1}+q_{k-1})^2+q_{k-1}^2}{4(\alpha_{k-1}+q_{k-1})^2\alpha_{k-1}q_{k-1}} > 0, \ \frac{(\alpha_{k-1}+q_k)^2+q_k^2}{4(\alpha_k+q_k)^2\alpha_k q_k} > 0, \\ &\frac{(\alpha_{k+1}+q_{k+1})^2+q_{k+1}^2}{4(\alpha_{k+1}+q_{k+1})^2\alpha_{k+1}q_{k+1}} > 0, \end{aligned}$$

when neglecting the motor model parameter uncertainties.

IV. Simulation Results and Performance Evaluation

In this section, the performance of the proposed SMC method is compared to hysteresis current controller in terms of RMSE current and torque, RMS current and torque ripple, which are defined as

$$I_{RMSE} = \sqrt{\frac{1}{\theta_p}\int_0^{\theta_p} (i_{ref} - i_k)^2 \mathrm{d}\theta}, \tag{17}$$

$$I_{RMS} = \sqrt{\frac{1}{\theta_p}\int_0^{\theta_p} i_k^2 \mathrm{d}\theta}, \tag{18}$$

$$T_{RMSE} = \sqrt{\frac{1}{\theta_p}\int_0^{\theta_p} (T_{e-ref} - T_e)^2 \mathrm{d}\theta}, \tag{19}$$

$$T_{rip} = \frac{T_{max} - T_{min}}{T_{ave}}, \tag{20}$$

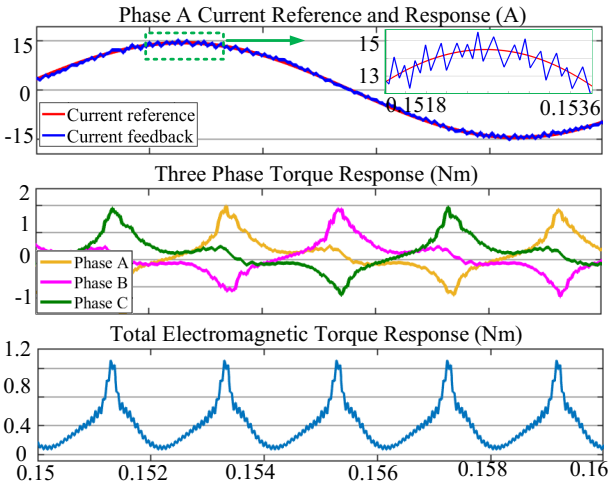

(a) $f_s \approx 10$ kHz,$f_c = 20$ kHz.

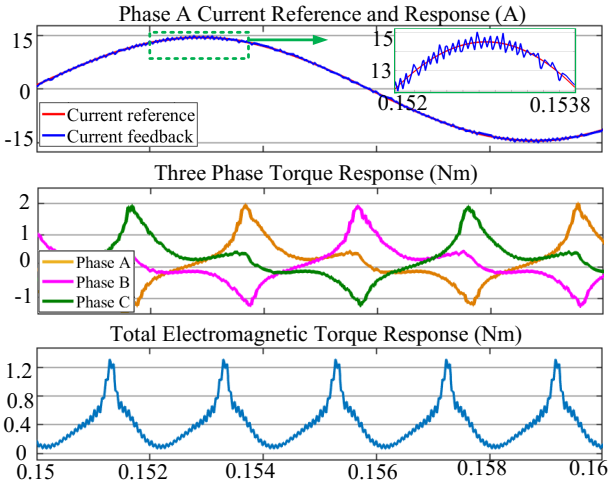

(b) $f_s \approx 10$ kHz,$f_c = 100$ kHz.

Fig. 6 Simulation results with hysteresis current controller.

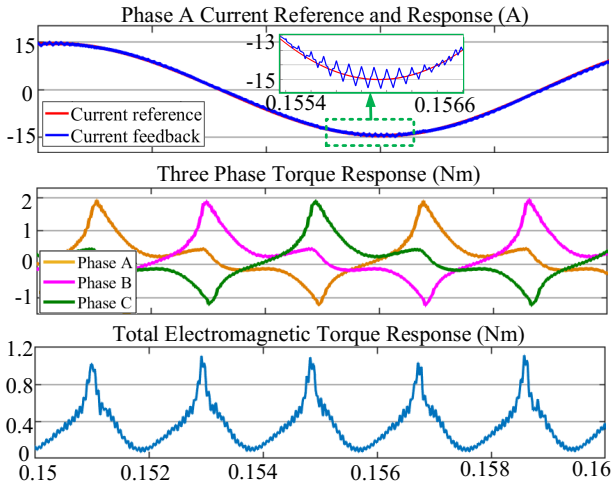

(a) $f_s = 10$ kHz,$f_c = 20$ kHz.

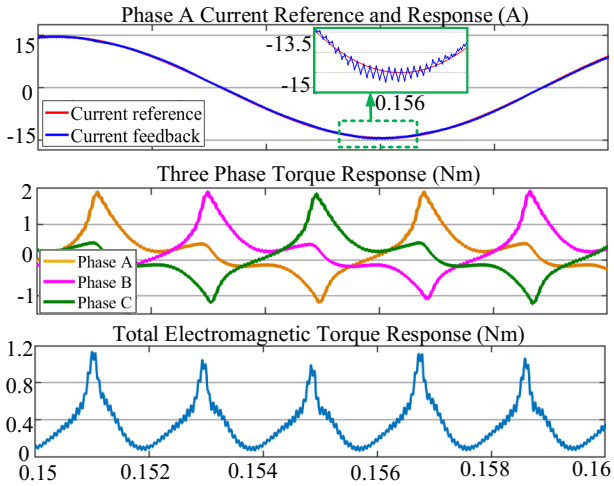

(b) $f_s = 20$ kHz,$f_c = 20$ kHz.

Fig. 7 Simulation results with sliding mode current controller.

where the pole pitch $\theta_p = 2\pi/N_p$ is determined based on the number of rotor poles. The current references are the three phase sinusoidal waveform given by

$$\begin{cases} i_{ref_{k-1}} = I_m \sin[N_p(\omega t - \delta)], \\ i_{ref_k} = I_m \sin[N_p(\omega t - 30^\circ - \delta)], \\ i_{ref_{k+1}} = I_m \sin[N_p(\omega t + 30^\circ - \delta)], \end{cases} \tag{21}$$

and the amplitude of the sinusoidal current reference is set to be 14.5 A and the leading angle is 1.5°.

The comparisons of the two current controllers are conducted twice under the switching frequency $f_s = 10$ kHz and $f_s = 20$ kHz, respectively. For the SMC, the controller parameters are set as $\alpha_{k-1} = \alpha_k = \alpha_{k+1} = 60,000, q_{k-1} = q_k = q_{k+1} = 10, \varepsilon_{k-1} = \varepsilon_k = \varepsilon_{k+1} = 10$ and $\alpha_{k-1} = \alpha_k = \alpha_{k+1} = 100,000, q_{k-1} = q_k = q_{k+1} = 1, \varepsilon_{k-1} = \varepsilon_k = \varepsilon_{k+1} = 100$, while the sampling rate remains as $f_c = 20$ kHz. For a fair comparison, first the current hysteresis band is set as 0.1A and the sampling rate f_c of the current feedback is set as 20 kHz to limit the switching frequency f_s around 10 kHz. Then, the sampling rate is set as 100 kHz and the current hysteresis band is set as 0.2 A to achieve an approximate 20 kHz switching frequency.

Figures 6 and 7 illustrate the current and torque trajectories with the two current controllers during the same time period. The MCSRM reaches higher speed of 1,275 rpm with SMC, while the one with hysteresis current controller reaches 1,220 rpm. Compared to the conventional hysteresis current controller, SMC achieves a constant switching-frequency current control for the MCSRM with comparable current tracking ability and lower sampling rate.

More comprehensive comparisons can be found in Table I. MCSRM with hysteresis current controller bears more significant torque ripples of around 340% and 370% when f_s is 10 kHz or 20 kHz, respectively, while MCSRM controlled by SMC under two sampling rates carries lower torque ripples of around 330% and 290%, respectively. Besides, the

TABLE I: Comparison of the performance of the two current controllers.

Speed (rpm)	Hysteresis current controller ($f_s \approx 20$k,$f_c = 100$k)				
	I_{RMS}	I_{RMSE}	T_{RMSE}	T_{ave}	T_{rip}
500	10.27	0.16	0.054	0.42	326%
1000	10.23	0.17	0.047	0.42	363%
2000	10.26	0.39	0.16	0.47	328%
3000	10.01	1.47	0.43	0.72	330%
Speed (rpm)	Hysteresis current controller ($f_s \approx 10$k,$f_c = 20$k)				
	I_{RMS}	I_{RMSE}	T_{RMSE}	T_{ave}	T_{rip}
500	10.19	0.33	0.062	0.43	372%
1000	10.22	0.36	0.072	0.42	373%
2000	10.21	0.58	0.19	0.47	369%
3000	9.84	1.53	0.40	0.71	380%
Speed (rpm)	Sliding mode current controller ($f_s = 20$k,$f_c = 20$k)				
	I_{RMS}	I_{RMSE}	T_{RMSE}	T_{ave}	T_{rip}
500	10.28	0.21	0.046	0.43	351%
1000	10.24	0.22	0.038	0.44	347%
2000	10.1	0.50	0.10	0.48	315%
3000	9.82	1.52	0.34	0.68	312%
Speed (rpm)	Sliding mode current controller ($f_s = 10$k,$f_c = 20$k)				
	I_{RMS}	I_{RMSE}	T_{RMSE}	T_{ave}	T_{rip}
500	10.25	0.10	0.032	0.45	311%
1000	10.24	0.16	0.041	0.46	306%
2000	10.09	0.68	0.14	0.53	268%
3000	9.59	1.93	0.39	0.73	293%

torque RMSE for the SMC-based controlled system is lower compared to the hysteresis-current-control-based system under the same switching frequency. Additionally, the data shown in the table also demonstrates that with the same switching frequency, both methods yield comparable current RMS around 10.25 A which agrees with the theoretical analysis. However, the current RMSEs for both methods increase significantly over 2,000 rpm. Furthermore, decreasing the sampling rate will worsen performance for both controllers, causing higher current ripples and torque fluctuations. Data provided in Table I compares the performance when the sampling rate is decreased from 100 kHz to 20 kHz for hysteresis current controller, where the current RMSE rises from averaged 0.55 A to 0.7 A and torque ripple from 340% to 370%. With the same switching frequency of 20 kHz, SMC scheme results in a more robust performance. To summarize, SMC offers advantages over hysteresis current control in terms of fixed switching frequency and lower sampling rates.

V. Conclusion

In this paper, the mathematical modeling and analysis revealed that the standard three phase VSC used for the investigated short-pitched MCSRM helps reduce the switching frequency compared to the conventional asymmetric bridge converter. The integral sliding mode control method was proposed in this work for the current control system aiming to achieve a fixed switching rate and lower sampling rate. The stability analysis of the closed-loop system with SMC and the parameter selection of the SMC was provided. Simulation results comparing to the hysteresis current controller validated the effectiveness and advantages of sliding mode control in terms of constant switching frequency and lower sampling rates. For the future work, further investigation is needed to reduce the torque and current ripples for the investigated MCSRM drive system.

Acknowledgment

This work is partially supported by NSF-ECCS-1725636 and NSF-ECCS-1851875.

References

[1] F. Peng, J. Ye, and A. Emadi, "A digital PWM current controller for switched reluctance motor drives," *IEEE Transactions on Power Electronics*, vol. 31, no. 10, pp. 7087–7098, 2016.

[2] J. Ye, B. Bilgin, and A. Emadi, "An offline torque sharing function for torque ripple reduction in switched reluctance motor drives," *IEEE Transactions on Energy Conversion*, vol. 30, no. 2, pp. 726–735, 2015.

[3] J. Ye, P. Malysz, and A. Emadi, "A fixed-switching-frequency integral sliding mode current controller for switched reluctance motor drives," *IEEE Journal of Emerging and Selected Topics in Power Electronics*, vol. 3, no. 2, pp. 381–394, 2015.

[4] J. Ye, B. Bilgin, and A. Emadi, "An extended-speed low-ripple torque control of switched reluctance motor drives," *IEEE Transactions on Power Electronics*, vol. 30, no. 3, pp. 1457–1470, 2014.

[5] G. Li, J. Ojeda, E. Hoang, M. Lécrivain, and M. Gabsi, "Comparative studies between classical and mutually coupled switched reluctance motors using thermal-electromagnetic analysis for driving cycles," *IEEE Transactions on magnetics*, vol. 47, no. 4, pp. 839–847, 2011.

[6] W. Ding, Y. Hu, and L. Wu, "Investigation and experimental test of fault-tolerant operation of a mutually coupled dual three-phase srm drive under faulty conditions," *IEEE Transactions on Power Electronics*, vol. 30, no. 12, pp. 6857–6872, 2015.

[7] R. Pupadubsin, N. Chayopitak, S. Karukanan, P. Champa, P. Somsiri, and K. Tungpimolrut, "Comparison of winding arrangements of three phase switched reluctance motor under unipolar operation," in *2012 15th International Conference on Electrical Machines and Systems (ICEMS)*. IEEE, 2012, pp. 1–4.

[8] J. Ye and F. Hensley, "Torque ripple and copper loss minimization for a family of mutually coupled switched reluctance machines," in *2017 IEEE Applied Power Electronics Conference and Exposition (APEC)*. IEEE, 2017, pp. 546–551.

[9] A. C. Clothier, "Switched reluctance motor drives with fully pitched windings," Ph.D. dissertation, Newcastle University, 2001.

[10] F.-C. Lin and S.-M. Yang, "Instantaneous shaft radial force control with sinusoidal excitations for switched reluctance motors," *IEEE Transactions on Energy Conversion*, vol. 22, no. 3, pp. 629–636, 2007.

[11] V. Rallabandi, S. Mallampalli, R. Rahul, and D. Torrey, "Performance comparison of switched reluctance motor with sinusoidal and conventional excitation," in *2015 IEEE Energy Conversion Congress and Exposition (ECCE)*. IEEE, 2015, pp. 5580–5585.

[12] X. Liang, G. Li, J. Ojeda, M. Gabsi, and Z. Ren, "Comparative study of classical and mutually coupled switched reluctance motors using multiphysics finite-element modeling," *IEEE Transactions on Industrial Electronics*, vol. 61, no. 9, pp. 5066–5074, 2013.

[13] M. Falahi and F. R. Salmasi, "A sliding mode controller for switched-reluctance motor with iterative learning compensation," in *2007 International Conference on Electrical Machines and Systems (ICEMS)*. IEEE, 2007, pp. 631–635.

[14] S. Sahoo, S. Panda, and J. Xu, "Direct torque controller for switched reluctance motor drive using sliding mode control," in *2005 International Conference on Power Electronics and Drives Systems*, vol. 2. IEEE, 2005, pp. 1129–1134.

[15] M. N. Isfahani, S. Saghaian-Nejad, A. Rashidi, and H. A. Zarchi, "Passivity-based adaptive sliding mode speed control of switched reluctance motor drive considering torque ripple reduction," in *2011 IEEE International Electric Machines & Drives Conference (IEMDC)*. IEEE, 2011, pp. 1480–1485.

[16] K. Hu, J. Ye, M. Velni, L. Guo, and B. Yang, "A fixed-switching-frequency sliding mode current controller for mutually coupled switched reluctance machines using asymmetric bridge converter," in *IEEE Transportation Electrification Conference and Expo*, 2019.